Editors' Suggestion | Featured in Physics

Vortex dynamics and fin-fin interactions resulting in performance enhancement in fish-like propulsion

Jiacheng Guo (郭佳诚),[1] Pan Han (韩攀),[1] Wei Zhang (张伟),[1] Junshi Wang (王君实),[1,*] George V. Lauder,[2] Valentina Di Santo,[3] and Haibo Dong (董海波)[1,†]

[1]*Department of Mechanical and Aerospace Engineering, University of Virginia, Charlottesville, Virginia 22903, USA*

[2]*Museum of Comparative Zoology, Harvard University, Cambridge, Massachusetts 02138, USA*

[3]*Division of Functional Morphology, Department of Zoology, Stockholm University, SE-11418 Stockholm, Sweden*

(Received 5 December 2022; accepted 2 June 2023; published 21 July 2023)

The leading-edge vortex (LEV) formation on the caudal fin (CF) has been identified as playing a key role in efficient lift-based thrust production of fish-like propulsion. The enhancement of the CF LEV through its interaction with vortices formed upstream due to a median fin with a distinct shape is the focus of this paper. High-speed, high-fidelity videos and particle imaging velocimetry (PIV) were obtained from rainbow trout during steady forward swimming to visualize the undulatory kinematics and two-dimensional flow behavior. Body kinematics are quantified using a traveling-wave formulation that is used to prescribe the motion of a high-fidelity three-dimensional surface model of the fish body for a computational fluid dynamics (CFD) study. The pressure field of the CFD result is compared and validated with the PIV result from the experiment. Using CFD, the vortex forming and shedding behaviors of the anal fin (AF) and their capturing and interaction with the trunk (TK) and the CF are visualized and examined. Coherent AF-bound LEVs are found to form periodically, leading to thrust production of the AF. The vortices subsequently shed from the AF are found to help stabilize and reinforce the LEV formation on the CF by aiding LEV initiation at stroke reversal and enhancing LEV during a tail stroke, which leads to enhancement of lift-based thrust production. The CF is found to shed vortex tubes (VTs) that create backward-facing jets, and the ventral-side VT and the associated backward jets are both strengthened by vortices shed by the AF. An additional benefit of the AF is found to be reduction of body drag by reducing the lateral crossflow that leads to loss of beneficial pressure gradient across the body. Through varying AF-CF spacing and AF height, we find that CF thrust enhancement and TK drag reduction due to the AF are both affected by the position and size of the AF. The position and area of the AF that led to the most hydrodynamic benefit are found to be the original, anatomically accurate position and size. In this paper, we demonstrate the important effect of vortex interaction among propulsive surfaces in fish-like propulsion.

DOI: 10.1103/PhysRevFluids.8.073101

[*]Present address: Department of Mechanical and Aerospace Engineering, Princeton University, Princeton, New Jersey 08544, USA.

[†]hd6q@virginia.edu

I. INTRODUCTION

The formation of leading-edge vortices (LEVs) has been observed to play a crucial role in the propulsive performance of wings and fins undergoing flapping (pitching) or oscillatory (combined heaving and pitching) motion [1–6]. In a computational study, Borazjani and Daghooghi [7] revealed that the oscillatory motion of the fish caudal fin (CF) creates prominent LEVs consistently over a variety of fish fin shapes. In the study of oscillating hydrofoil by Lighthill [2], it is found that fish swimming with high hydromechanical efficiency balance the two mechanisms of force production: (1) the forward component of pressure difference between the two sides of the fin and (2) the leading-edge suction due to the low-pressure region created by the swirling of water around the leading edge. This suction force created by leading-edge vorticity, clearly visualized computationally in the review study of LEV formation on moving plates by Eldredge and Jones [4], is a well-known mechanism by which birds and insects augment their lift production [5,8–11]. Anderson *et al.* [1], studying the performance of oscillating hydrofoil, found that high propulsive efficiency is related to the formation of moderately strong LEVs on alternating sides of the foil.

The suction force created by a LEV is dependent on its circulation strength [4]. To explore methods of enhancing the LEV circulation and stability, Harbig *et al.* [9] conducted a computational study on a flapping plate and found that the attachment and circulation of a LEV can be enhanced by an increase in advance ratio, based on a definition like the Strouhal number. However, whether the LEV enhancement came at a cost of increased power consumption is not discussed, even though in oscillating foils and fish swimming, Strouhal number changes have been found to affect propulsive efficiency [1,3]. For ways to enhance both the LEV and propulsive efficiency simultaneously, there is growing interest in vortex capturing in fish-inspired locomotion [6,12–20]. Liao *et al.* [12,13] found that, by introducing vortices upstream of a live trout, the trout would adopt a gait synchronized to the upstream vortex shedding and trace the path of the vortices, a locomotion pattern that is associated with energy recovery. Experimental and computational studies of hydrofoils in tandem formation undergoing either pure pitching or oscillation motions found that the performance of the downstream foil is affected by the vortex pattern it encounters [15,16,18,20–27]. In the study by Newbolt *et al.* [24] in which tandem hydrofoils were assigned uncoordinated flapping motions, the follower in the wake of the leader could fall into various stable positions controlled by changes in amplitude, phase, and frequency. Akhtar *et al.* [16] conducted a computational bio-inspired tandem foil study, wherein the motion of the two foils is prescribed based on the motion of the dorsal fin (DF) and CF in a bluegill sunfish, finding a unique mechanism of thrust enhancement whereby the upstream fin alters the flow so that the downstream fin exhibits a larger angle of incidence, and thus, the formation and shedding of a LEV on the downstream fin is enhanced. In the study by Zhang *et al.* [25] of fin-fin interaction using tuna-inspired fin models and kinematics, it was found that the LEV-based thrust production of the CF was enhanced through encountering the same-signed vortex shed from the upstream fin. In a computational study of periodically pitching tandem foils, Han *et al.* [19] observed LEV enhancement in the downstream foil and achieved a multifold efficiency boost by adjusting the relative flapping phases of the foil. Han *et al.* [19] also identified four main wake types containing combinations of 2-S and 2-P vortices and their associated mean-flow jet shapes, finding the 2-P vortices, formed due to the optimal combining of the LEV and trailing-edge vortex (TEV) of the hindmost foil, to be the most closely associated with high propulsive efficiency. The optimal vortex capturing of a downstream foil and the propulsive performance of the whole system can depend on both the relative oscillating phase difference and the spacing between the two foils [15,18,24,25]. In the study by Zhang *et al.* [25], constructive fin-fin interaction was achieved across a wide range of spacing and phase variations, with the interaction tending to be stronger in close formations and when the upstream fin was leading in phase. In a study focusing on the hydrodynamic energy recovery of oscillating foils, Kinsey and Dumas [18] found that the optimal positioning of the foils for energy recovery can be characterized by a global-phase parameter that accounts for both the oscillating phase difference and the spacing between the two foils. Ribeiro *et al.* [15] combined experimental and computational approaches and modified the global phase by also accounting for the interfoil flow velocity to achieve a better prediction of the efficiency of the

downstream foil and the associated energy efficiency. Overall, it is found that both foils produce thrust, and the propulsive efficiency of the downstream foil is optimized when the capturing of incoming vortices enhances the LEV circulation of the downstream foil.

Observation from real fish swimming supports the hypothesis of fish propulsion benefiting from fin-fin interaction [28–31], as tandem-foil studies predict. However, it is unclear from these observations if findings from tandem-foil studies are directly applicable to real fish swimming. Pure tandem-foil configurations often neglect the existence of a trunk (TK), which can restrict foil kinematics and alter the flow in ways unaccounted for. Matthew and Lauder [32] navigated the existence of a TK by constructing pitching-heaving plates specifically shaped to mimic the entire sideview silhouette of a fish containing median fins and CFs with different spacings. A larger change in performance is observed in plates with varying flexibility than in plates with varying fin-fin spacing. Computationally, Liu *et al.* [6] and Han *et al.* [33] studied the fin-fin and fin-body interactions of the median fin, TK, and CF using realistic three-dimensional (3D) models and undulating kinematics of jackfish and sunfish, respectively. By constructing three different models (full-body model, model with TK and CF and without median fins, and caudal-fin-only model), the effect of fin-fin interaction on the propulsive performance of the CF was isolated, and Liu *et al.* [6] found that the CF thrust and LEV are enhanced by the presence of the median fins, which extend and redirect TK-bound vortices to be better accessed by the CF for its own LEV formation. By varying the relative phase difference between the median fin and CF, Han *et al.* [33] found that the phase-lead exhibited by the median fins can better enhance the CF LEV. However, in both cases, differing from the thrust-producing leading foils in tandem-foil studies, the median fins serve only to extend the vortices that originate on the TK, and no median-fin propulsive performance or vortex generation independent of the TK was discussed.

In this paper, we aim to further elucidate the flow physics behind the enhancement of the LEV due to fin-fin interactions and its benefits to performance in both thrust production and energetics, using a realistic trout-like model which exhibits an anal fin (AF) that extends far and has a shape distinct from the outline of the TK, allowing it to interact with the flow more directly than jackfish and sunfish. In experimental studies of trout swimming, the AF is found to produce reverse von-Karman wake patterns [29,30], the interactions of which with the CF and associated performance enhancement can be interesting areas of discussion. The analysis showcased in this paper combines experimental and computational approaches, using experimental data on the live fish as the basis for extensive computational modeling, focusing on the interactions between the AF and CF. We obtained particle imaging velocimetry (PIV) data from fish swimming in a flow tank, and then flow simulation studies are conducted on a realistic 3D TK and fin model whose motion is based on the video recording of the fish swimming during the PIV data collection. The simulation results are validated with the PIV data to ensure compatibility to experiments and then used to resolve detailed flow physics and vortex dynamics. The body kinematics are governed by a traveling-wave (TW) model [33]. This TW reconstruction approach produces symmetric kinematics, somewhat simplified from the actual fish motion, that can be reduced to parametric components and easily replicated. The TW kinematics is validated against the recorded fish kinematics to ensure good agreement between the model and true kinematics.

The spacing between the AF and CF is varied to study its effectiveness at different positions along the body. Fish species in general and trout species particularly differ in the location of the AF relative to the tail, and a computational approach allows for the fine control of such a parameter. In addition, the aspect ratio (AR) of the AF is varied to mimic the opening and closing of the AF observed during fish locomotion. The outcome of this paper is a characterization of flow physics involved in the interaction between the distinctive median fin and CF of the trout, both exhibiting unique shapes that produce vortex structures and interactions previously undiscussed, leading to a more complete understanding of LEV-based thrust and propulsive efficiency enhancement through vortex interactions. This combination of experimental data from live fish and computational simulations is also conducive to designing efficient biomimetic fish-like robots and Autonomous Underwater Vehicles (AUV) [34,35].

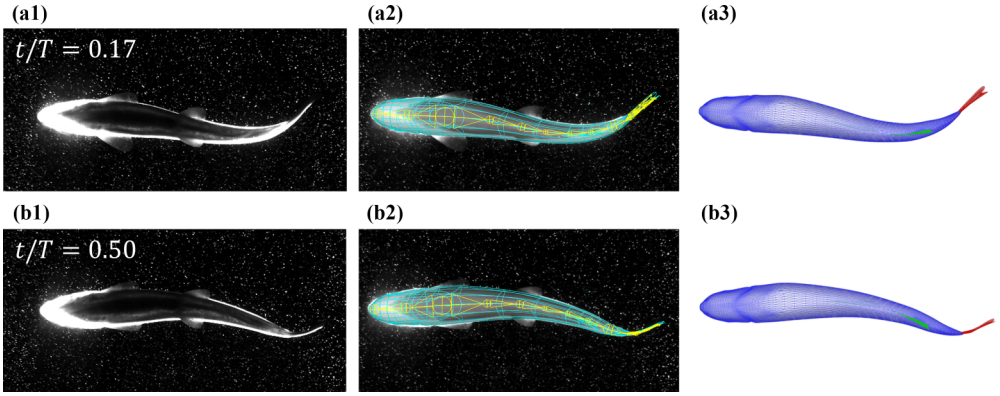

FIG. 1. (a1) and (b1) Original frames from the video recording taken during particle imaging velocimetry (PIV) data collection. (a2) and (b2) Surface mesh (coarsened and untriangulated for visualization) is highlighted in cyan, while the virtual skeleton is highlighted in yellow. (a3) and (b3) Fully refined and triangulated surface mesh of the fish trunk (blue) and two-dimensional membrane bodies representing the caudal fin (CF, red), anal fin (AF, green), and dorsal fin (DF, green).

The organization of subsequent sections is as follows. Section II A describes the setup of experiments for PIV data collection and video recording. Section II B describes the computational model and body kinematics. Section II C describes the simulation setup and flow solver. The results of the PIV-computation validation are shown in Sec. II C. Section III A compares the hydrodynamic performance and vortex structures of the full-body model (M1) and the model without the AF (M2). Sections III B and III C, respectively, compare the performance and vortex structures among models with varying spacing between the AF and CF and among models with varying AF ARs.

II. METHODOLOGY

A. Setup for experimental data collection

Experiments on live rainbow trout (*Oncorhynchus mykiss*) swimming steadily included video recording and PIV data acquisition. The fish swam in a recirculating flow tank using setups described in studies conducted by Drucker and Lauder [30], Standen and Lauder [29], Matthews and Lauder [32], and Di Santo *et al.* [36]. Briefly, live fish 11–15 cm in body length swam against an imposed flow that ranged from 0.5 to 2.0 body lengths per second (L_B/s) in a flow tank with cross-sectional area of 30 cm^2 and a working section length of 100 cm. Three synchronized high-speed cameras (Photron mini-AX200, 1024×1024-pixel resolution) were used to capture swimming kinematics of both the body and AF from the lateral, ventral, and posterior views at 250 frames per second. Posterior-view video visualization of the deformation and relative phase difference between fins were aided by a mirror using a setup described in Refs. [28,37,38]. Small near-neutrally buoyant 50-μm particles were added to the recirculating flow tank and illuminated with two 5 W argon ion lasers (Optoengine Inc.). Use of two lasers, one illuminating the body from the left side and the other from the right side, minimized regions with poor illumination. The particle flow over the fish was visualized with a ventral view camera at 1280×1024-pixel resolution filming at a rate of 1000 frames per second. The resulting high-speed videos of particle flow patterns were analyzed using Davis v8.3 software (LaVision Inc.) using the same parameters as in recent studies of aquatic locomotion [32,39–41]: 50% interrogation window overlap and sequential image cross-correlation.

High-fidelity reconstruction of the undulatory kinematics of the fish swimming is done based on the video recording of a representative undulating cycle. A selection of frames of video recording during such an undulating cycle are shown in the ventral view in Figs. 1(a1) and 1(b1). On Autodesk Maya, an anatomically realistic virtual skeleton and 3D surface model are constructed

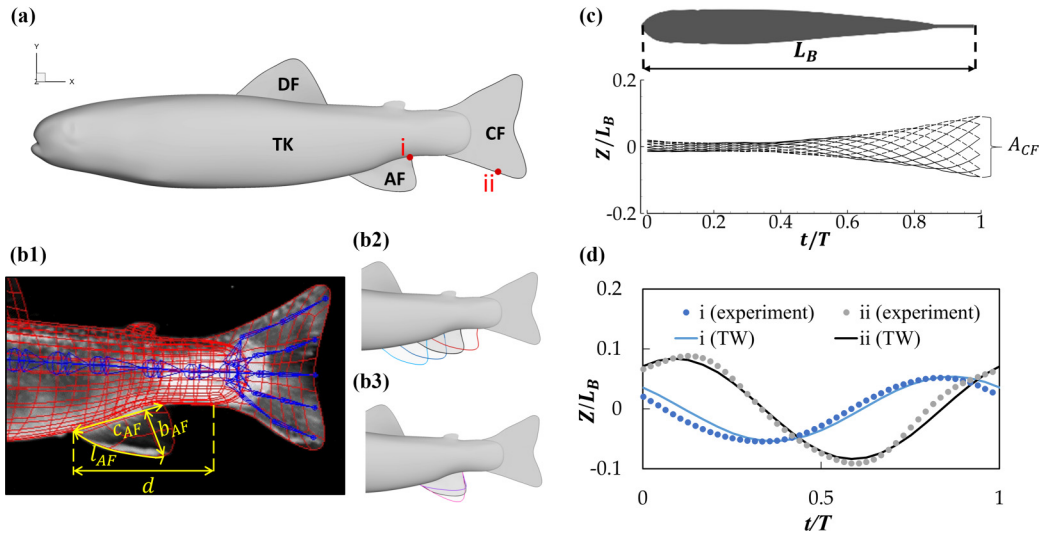

FIG. 2. (a) Lateral of the computational model with abbreviations of body parts labeled. (b) Parametric study setup with (b1) defining key geometric parameters on a coarse mesh model overlaid on a picture of the real fish, (b2) demonstrating cases of varying the anal fin (AF)-caudal fin (CF) spacing d to 1.5 (cyan), 1.25 (blue), and 0.75 (red) times the original position d_0. (b3) Parametric study cases of varying the AF aspect ratio through variations of b_{AF} to 0.75 (purple) and 1.25 (red) times the original. (c) Midline kinematics generated by the traveling-wave (TW) model. (d) Validation of the TW model by tracking two points [labeled in (a)] in an entire undulation cycle, solid lines representing the TW kinematics and dots representing measurements based on the video recording (experimental).

based on the individual fish in the video recording. A Catmull-Clark subdivision method used in the meshing of the 3D surface and membranes ensures the smoothness of the surfaces of the fish model. Figures 1(a2) and 1(b2) show a basic, rectangular surface mesh that subdivides the TK surface. This rectangular mesh is then further subdivided, refined, and triangulated to achieve the computationally robust 3D mesh shown in Figs. 1(a3) and 1(b3). The accuracy and compatibility of the current triangular surface mesh and computational solver are described in more detail in Ref. [42]. A skeleton-based method with calibration in a virtual scene, a technique proven accurate in reconstruction of the kinematics of jackfish undulation [6] and hummingbird flapping [43], is used for the undulatory kinematics reconstruction. The accuracy of this reconstruction method has been studied and described in detail by Koehler *et al.* [44]. The virtual skeleton, set up based on fish anatomy with individual vertebral segments along the body axis, allows for finetuning of minute deformations of the 3D model, including the bending of the TK and the axial twisting of the CF shown in Figs. 1(a1)–1(a3). Rigging the virtual skeleton to the surface mesh resulted in the deformed model shown in Figs. 1(a3) and 1(b3), in good agreement with the fish in the original recording.

B. Fish-like TK-fin model kinematics

For the computational study, the 3D model of the fish, shown in lateral view in Fig. 2(a), includes the TK, CF, DF, and AF. The TK is modeled as an enclosed surface body, while the fins are modeled as membranes, like the modeling techniques employed by Liu *et al.* [6]. The body undulation kinematics reconstructed from video recording is modeled using a TW formulation to quantify key characteristics in the undulating motion. The kinematics generated from the TW model is then validated against the reconstructed kinematics to ensure accuracy. Parametric studies are set up to study the effect of varying positions and sizes of the AF on its effectiveness and interaction with other body parts. The TW undulation model allows for the modeling of the AF motion even when

TABLE I. Relevant geometric parameters of the fish.

L_B	$\frac{S_{DF}}{L_B^2}$	$\frac{S_{AF}}{L_B^2}$	$\frac{S_{CF}}{L_B^2}$	$\frac{d_0}{L_B}$	$\frac{b_{AF_0}}{L_B}$	$\frac{A_{CF}}{L_B}$
11 cm	0.011	0.0065	0.022	0.194	0.0634	0.19

its position and shape are modified. The details of the modeled undulating kinematics, its validation, and the setup of the parametric study are discussed in more detail below in this section.

Table I summarizes the key geometric parameters of the fish model, in which L_B represents the total body length of the fish, and S_{DF}, S_{AF}, and S_{CF} represent surface areas of DF, AF, and CF. AF-CF spacing is defined as the longitudinal distance (measured along the TK centerline) between the leading-edge roots of the AF and CF and represented by d, as shown in Fig. 2(b1). The AF-CF spacing of the baseline model is represented by d_0. Similarly, b_{AF} represents the AF span, while b_{AF0} represents the AF span in the baseline model. The AF span is taken as the largest distance between the base (the line of intersection between the AF and TK) and the outer edge of AF. Here, A_{CF} represents the tip-to-tip flapping amplitude of the CF, defined in Fig. 2(c).

The TW equation that governs the undulation motion of the TK and CF is Eq. (1), with the term $a(x)$, defined by Eq. (2), a parabolic equation that defines the excursion envelope of the undulation:

$$z(x,t) = a(x)\sin\left(\frac{2\pi}{\lambda}x - 2\pi ft\right), \tag{1}$$

$$a(x) = Ax^2 + Bx + C. \tag{2}$$

Here, $z(x,t)$ is the lateral excursion of a station along the fish body, as a function of x, the distance measured from the snout in the longitudinal direction when the fish is in a straightened shape, and t, time since the beginning of the current undulatory cycle. Equation (1) then describes the lateral position of a station (given by x) along the midline of the fish at a given time. Both $z(x,t)$ and x take units of L_B. In the parabolic equation, $a(x)$ has coefficients $A = 0.127$, $B = -0.050$, and $C = 0.0177$. The parameter λ is the undulatory wavelength of the body of the fish. Different fish exhibit generally similar kinematic patterns regardless of body shape and undulatory modes, with wavelengths ranging from $0.50L_B$ to $1.50L_B$ [36]. For the model fish in this paper, λ of $0.8L_B$ is found to produce kinematic patterns that are the most representative of the original kinematics, which is typical of a carangiform swimmer like trout [45]. The undulating frequency f is normalized to be 1. With the parameters given here, Fig. 2(c) shows the midline kinematics generated by the TW formulation. The outer edges trace the parabolic curve given by Eq. (2). The projected length of the fish model is kept constant. This formulation does permit the length of the fish model to change slightly while undulating, but the variation is kept at a minimum. The instantaneous midline length L is calculated at 48 discrete timesteps during a cycle, producing a cycle average value $\bar{L}$ of 1.029, maximum value L_{max} of 1.037, and minimum value L_{min} of 1.021. The range of variation $(L_{max} - L_{min})/\bar{L} < 1.6\%$. With the same method, previous works have achieved realistic fish motions and hydrodynamics [46,47].

The median fins, AF, and DF are assigned the same frequency f as that of the TK and CF. In this paper, to maintain lateral symmetry of the undulating kinematics and focus on the effect of hydrodynamic interaction between the AF and CF, the median-fin membranes are allowed to move passively due to the motion and curvature of the specific sections of the TK on which the median fins are attached. To validate the TW kinematic model, two points are selected [points (i) and (ii) in Fig. 2(a)], on the TK and CF, at stations $x = 0.75L_B$ and $0.94L_B$, to be tracked from the video-recording-generated kinematics for a complete cycle. The tracked results are plotted in Fig. 2(d) and compared with the TW equation curve. The comparison shows good agreement between the kinematics directly derived from experiments and the estimation using the equation.

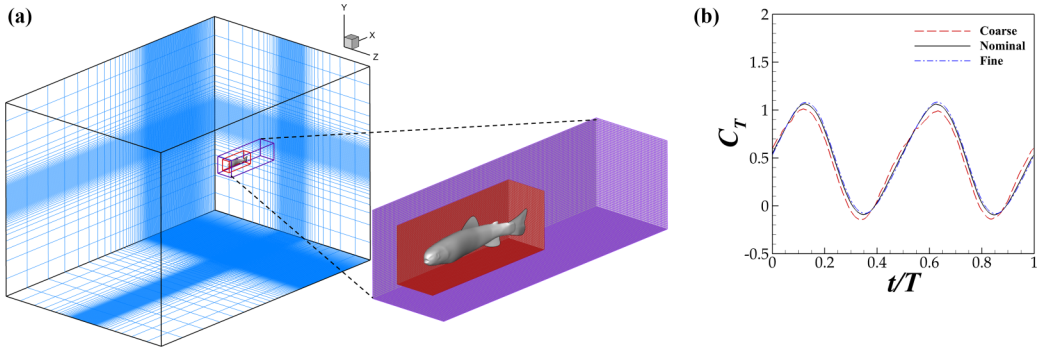

FIG. 3. Computation grid setup: (a) Nominal Cartesian grid with base mesh and nested adaptive mesh refinement (AMR) blocks, with a total grid count of 12 million. Every second grid point is shown for visibility. (b) Grid-dependence study with instantaneous C_T for reconstructed kinematics for a fine grid (20 million grid points), a coarse grid (7 million grid points), and the nominal grid (12 million grid points) used for subsequent analysis.

The CF-tip flapping amplitude A_{CF} in the TW model is $0.19L_{\mathrm{B}}$. The nondimensionalized parameters, Strouhal number (St) and Reynolds number (Re) are calculated using U_∞ as the incoming flow velocity relative to the fish and ν as the kinematic viscosity:

$$\mathrm{St} = \frac{fA_{\mathrm{CF}}}{U_\infty}, \quad \mathrm{Re} = \frac{U_\infty L_{\mathrm{B}}}{\nu}. \tag{3}$$

The fish in the experiment modeled here exhibited St and Re of ∼0.47 and 16 000, and the fish model used for the computational study exhibited St and Re of 0.47 and 4000. For validation of the computational fluid dynamics (CFD) solver against PIV data, a higher Re of 8000 is used in the simulation. The Re used in the computational study is smaller than that encountered by the real fish to strike a balance between computational load and wake resolution. In the studies by Han *et al.* [33] and Liu *et al.* [6], it is found that the primary wake structure is well developed with the Re regime used in this paper.

Two parametric studies are set up, visualized by Figs. 2(b2) and 2(b3). By varying the location of the AF, shown in Fig. 2(b2), the effect of AF-CF proximity and spacing on fin-fin interaction is studied, and by adjusting the AF height b_{AF}, shown in Fig. 2(b3), while keeping the leading-edge arc length (l_{AF}) constant, the effect of the opening and closing of the AF rays is mimicked. In varying the location of the AF, care is taken to keep the base chord (c_{AF}), b_{AF}, and l_{AF} constant. The surface area of the AF (S_{AF}) variation is kept <4% to allow for reliable scaling of measured forces. The AF-CF spacing and AF height in the original unvaried model d_0 and b_{AF_0} are used as baseline for comparison.

C. Numerical solver

A computational domain of size $10L_{\mathrm{B}} \times 6L_{\mathrm{B}} \times 6L_{\mathrm{B}}$ is set up in a Euclidean space with an x-y-z coordinate system. The 3D fish model in this domain is oriented such that it faces the negative x direction, and its DF points in the positive y direction. A Cartesian mesh is used to discretize the domain spatially. A schematic of the discretized region is shown in Fig. 3(a), in which every second grid point is displayed to ensure visibility. A dense region with uniform grid spacing $\Delta x = \Delta y = \Delta z = 0.0128L_{\mathrm{B}}$ is set up around the body of the fish, as indicated in the dense blue region in Fig. 3(a). The flow region ahead of the snout of the 3D fish model is set to be $6.5L_{\mathrm{B}}$ to allow the upstream flow to fully develop, leaving a region of $2.5L_{\mathrm{B}}$ to capture the wake structure behind the tail, with a low stretching ratio of 0.65 such that the grid spacing at the outlet ($\Delta x = 0.08L_{\mathrm{B}}$) is small enough to resolve the vortices of comparable size in that region. Additionally, near field of

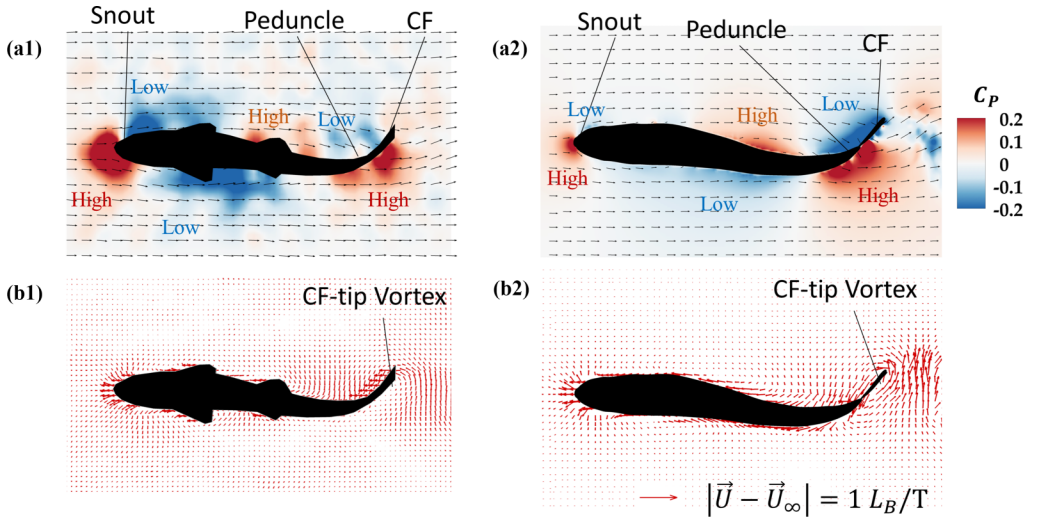

FIG. 4. (a) Pressure contour and (b) net velocity vector fields on a coronal slice cut at $t/T = 0.17$ showing (a1) and (b1) experimental [particle imaging velocimetry (PIV)] results and (a2) and (b2) computational fluid dynamics (CFD) results.

the body, two nested adaptive mesh refinement (AMR) blocks are used to further refine the dense mesh to resolve the pressure and viscous forces acting on the fish body. The positions and sizes of the AMR blocks near the body are signified by purple and red outlines in the base-mesh schematic in Fig. 3(a). A schematic of the mesh in the AMR region is also shown in Fig. 3(a). The innermost AMR block (red) fully bounds the fish body, and the intermediate AMR block (purple) fully contains the innermost block and extends another $1L_\mathrm{B}$ in the x direction to resolve the finer details of the immediate wake. The smallest grid spacing inside the AMR region is equal to $0.0032L_\mathrm{B}$, and the total grid count in the entire computational domain including the AMR blocks is 12 million.

To preclude the effect the grid density can have on the calculation of forces acting on the surface of the fish model, a grid-independent study is conducted on the nominal mesh described above, a coarse mesh with minimum grid spacing $\Delta x = 0.0064L_\mathrm{B}$ and a dense mesh with minimum grid spacing $\Delta x = 0.0024L_\mathrm{B}$. The thrust coefficient (C_T) of CF over an entire undulating cycle is calculated from simulations conducted on the three mesh setups, using Eq. (4):

$$C_T = \frac{-F_x}{0.5\rho U_\infty^2 S_\mathrm{CF}}, \tag{4}$$

where F_x is the x-directional force, with the thrust force pointing in the negative x direction, and ρ is the fluid density. The result is plotted in Fig. 3(b). In finding that a 25% refinement of grid spacing from the nominal to the dense mesh resulted in a 1.8% C_T peak value change, we conclude that the nominal mesh is good enough for the computation, and therefore, the subsequent analyses are conducted with this nominal mesh.

In this paper, we use a direct numerical solver (DNS) to calculate the Navier-Stokes equations and resolve the fluid behavior of the swimming fish model. The same solver has successfully resolved biological flows in various cases of animal locomotion around membranous and enclosed surfaces [5,6,10,23,48,49] and has been validated against PIV experiments in specific applications [35,50]. To verify that DNS used in this paper is effective in resolving the fluid behavior in the swimming of the fish, simulation results are compared with the PIV data that are used to estimate fish body surface pressure. The velocity vector fields generated from the PIV video recordings of fish swimming [Fig. 4(b1)] were processed according to the approach detailed in Refs. [39–41,51,52] to generate the distribution of body surface pressures shown in Fig. 4(a1). In the simulation domain, a slice cut

is made at a location relative to the fish model like the horizontal laser sheet relative to the fish body in the PIV data collection to produce the pressure and velocity vector fields shown in Figs. 4(a2) and 4(b2). In both cases, C_P, the coefficient of pressure, is calculated using $C_P = P/(0.5\rho U_\infty^2)$, where P is pressure.

There is overall good agreement between PIV and CFD results in capturing the locations and relative strengths of dominant pressure (red) and suction (blue) regions around the fish body, as seen in Figs. 4(a1) and 4(a2). A high-pressure region directly ahead of the snout persists throughout an entire cycle of undulation and is well captured consistently by both PIV and CFD results. This is the expected result of the exposed fish snout encountering the incoming flow, causing overall drag. At the fish peduncle-tail region, a pair of high- and low-pressure regions exists because of the undulation of the tail of the fish, whereby the tail applies a force on the fluid particles in its path and creates a relative vacuum in its immediate wake. Though the high- and low-pressure regions oscillate between the left and right sides of the fish peduncle-tail section due to the cyclic motion of the tail, the high-pressure (push) region remains relatively downstream, and the low-pressure (suction) region remains relatively upstream of the tail, creating a persisting net forward propulsive force as the tail undergoes each stroke. Corresponding to the high-pressure region at the snout of the fish in Figs. 4(a1) and 4(a2), an overall slowdown of the flow is observed in Figs. 4(b1) and 4(b2) in the same region. Along the fish body and CF, flow slowdown in the boundary layer is observed in both PIV and CFD results. Around the CF tip, flow from one side of the fin circulates to the other side, forming a CF-tip vortex, which is well captured by both PIV and CFD.

In addition to the high-pressure region near the snout and the paired low- and high-pressure regions near the peduncle-tail section, several other regions with prominent pressure values are scattered along the TK. The relative size and location of these regions compare well between PIV and CFD results. It should be noted that exact replication of the flow condition in the collection of PIV data was not feasible in the DNS simulation, whose Re is half the experimental value. Also, the body of the fish in the experiment includes the pectoral and pelvic fins that are excluded from the 3D model used in the computational study to focus on resolving the flow features relevant to AF-CF interaction. Therefore, perfect quantitative agreement between experiment and simulation is not expected. Nevertheless, our DNS produced a flow topology that matches well with the experiment, with values in the same order of magnitude, and therefore, the subsequent analyses are conducted with greater confidence using the DNS described in this section.

III. RESULTS AND DISCUSSION

A. Baseline performance and hydrodynamics

The time history of the coefficient of thrust (C_T) and coefficient of power consumption (C_{PW}) are shown in Fig. 5 for the TK, AF, and CF of M1 (TK + DF + AF + CF) and M2 (TK + DF + CF) for one entire undulating cycle. Here, C_T is calculated using Eq. (4), and C_{PW} is calculated using Eq. (5), where Pw is the hydrodynamic power consumption, calculated using $Pw = \oint -(\overline{\overline{\sigma}} \cdot \boldsymbol{n}) \cdot \boldsymbol{u}\, dS$, with $\overline{\overline{\sigma}}$ being the local stress tensor on a body surface element with an area of dS, $\boldsymbol{n}$ is the normal vector of the surface element, and $\boldsymbol{u}$ is the velocity vector of the surface element relative to the incoming flow:

$$C_{\mathrm{PW}} = \frac{Pw}{0.5\rho U_\infty^3 S_{\mathrm{CF}}}. \tag{5}$$

The gray region ($t/T \in [0.00,\ 0.50]$) signifies the rightward half stroke, during which the CF tip travels from left to right, and the white region signifies the leftward half stroke, during which the CF tip travels from right to left, ending up at the position where it originated from in the undulation cycle. The general trends are qualitatively similar between the two models. Affirming numerous previous studies, the CF is found to be the main propulsor, and the TK is drag producing. The AF at its current location is found to produce a small amount of thrust, 5.3% of total thrust in M1. AF thrust

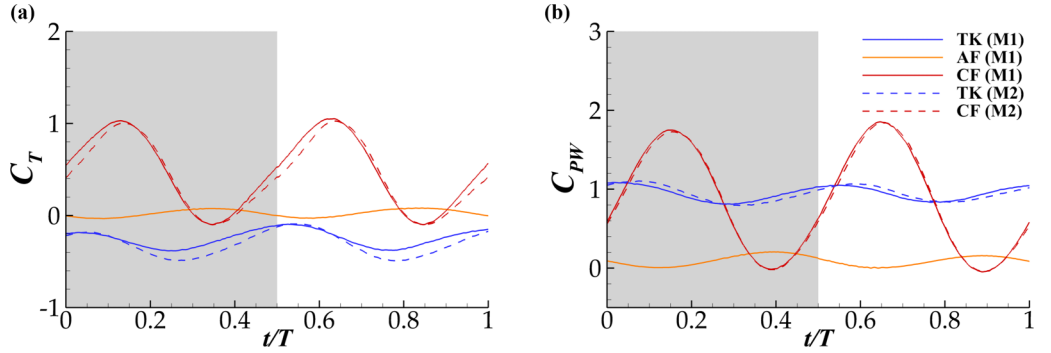

FIG. 5. Time history of (a) coefficient of thrust and (b) coefficient of power for M1 and M2 during one typical undulating cycle.

production can both contribute to propulsion in forward swimming and aid in maneuverability, as suggested by Standen and Lauder [29] and Drucker and Lauder [30]. The cycle-averaged values of the coefficients of thrust and power $\bar{C}_T$ and $\bar{C}_{\mathrm{PW}}$ are calculated. In one cycle, in the presence of AF, the CF of M1 produces more thrust (8.6%) than that of M2, and the TK of M1 produces less drag (18.6%) than that of M2. In terms of power consumption, the TK and CF of M1 experience marginally more hydrodynamic power consumption than the TK and CF of M2, by $<$0.1 and 1.3% respectively. The AF consumes 4.6% of total power in M1. Summing the effects of the TK, CF, and AF for M1 and the TK and CF for M2, the overall power consumption of M1 only exceeds M2 by 6%.

The most CF thrust enhancement due to the AF is found to occur in the region $t/T \in (0.38,\ 0.65)$, during stroke reversal, while drag reduction occurs in the region of $t/T \in (0.13,\ 0.50)$, during a stroke. A comparison of fluid flow and pressure fields focusing on these time periods can provide insight into the physics behind the AF's role in CF thrust enhancement and trunk drag reduction.

Toward unraveling the physics that lead to the thrust enhancement observed in Fig. 5(a), we examined the vortex structure in the wake and around the body of the fish, depicted in Figs. 6(a) and 6(b). The wake generated from two undulating cycles and vortices actively forming around the fish body in the third cycle are shown in Figs. 6(a) and 6(b). A double-row [53] wake structure is observed in Fig. 6(a), whereby vortex rings form at the tail and diverge laterally in the plane of undulation, typical of a carangiform swimmer at the current regime. Strong vortex cores form around the fish body. LEVs form on both the dorsal and ventral leading edges of the CF, as shown in Fig. 6(b). The AF vortex (AFV), formed due to the combining of the LEV and TEV formed at the AF, is shed at the AF tip, advected downstream, and caught by the leading edge of the CF to combine with its own LEV, as shown in Fig. 6(b). At the trailing-edge of the CF, TEVs are formed, and these connect with the LEVs to be shed together downstream. Typically, vortex rings or loops can form due to the linking of LEVs with each other and with TEVs and have been identified to be responsible for the propulsion of ray-fin fish swimming [31]. In the study by Liu *et al.* [6], vortex rings are clearly identified to contribute to creating thrust-producing backward-facing jets. In this paper, the wide peduncle and truncate CF of the trout, contrasting the narrow peduncle and forked CF of the crevalle jack, combined with differences in kinematics, may be responsible for the relatively laterally elongated vortex rings in the far wake shown in Fig. 6(a). Such an elongated vortex ring has prominent counterrotating vortex tubes (VTs) parallel to each other, formed due to LEV shedding from the CF leading edges. The paired VTs generate a strong backward-facing jet that is responsible for thrust production, as shown in Figs. 6(c) and 6(d). The strength of the backward-facing jet production in M1, shown in Fig. 6(c), is stronger than in M2, shown in Fig. 6(d).

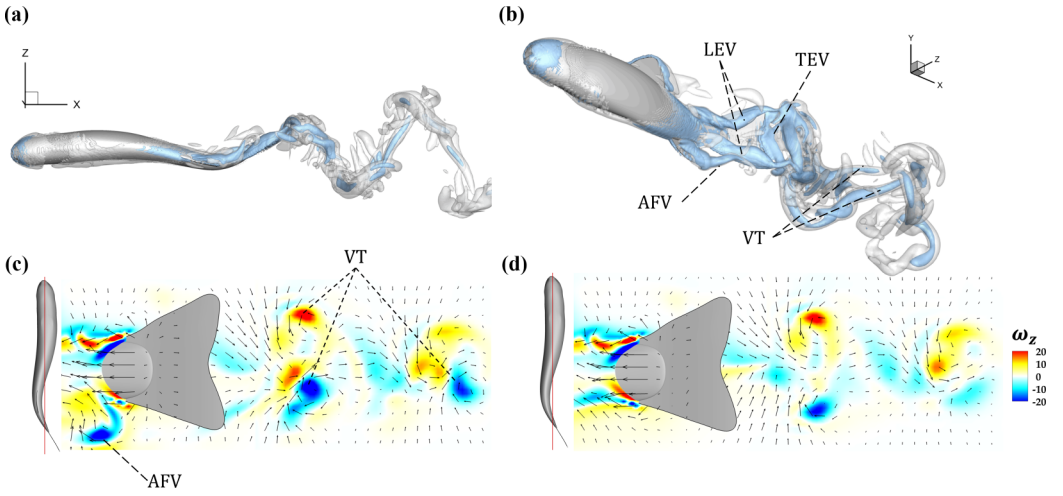

FIG. 6. Wake structure and vortex shedding with Q-criterion isosurfaces at $t/T = 0.18$ shown in (a) ventral view and (b) perspective view for $Q = 50$ (blue) and $Q = 5$ (white, transparent), and z vorticity ω_z of (c) M1 and (d) M2 at the plane denoted by the red line.

The formation of VTs is identified to be crucial in thrust production, through which the underlying reason for the enhancement of C_T due to the AF can be found.

To understand the capturing and interaction of different body parts and vortices that lead to the enhancement of thrust-producing VTs, the wake structures of M1 and M2 are depicted sequentially at various timesteps in Figs. 7 and 8, with the main vortices labeled. The red dashed lines trace the vortices with red arrows indicating the direction of rotation of the vortices using a right-handed system. Text labels of abbreviations of vortex names are attached to the red dashed lines. CF LEVs

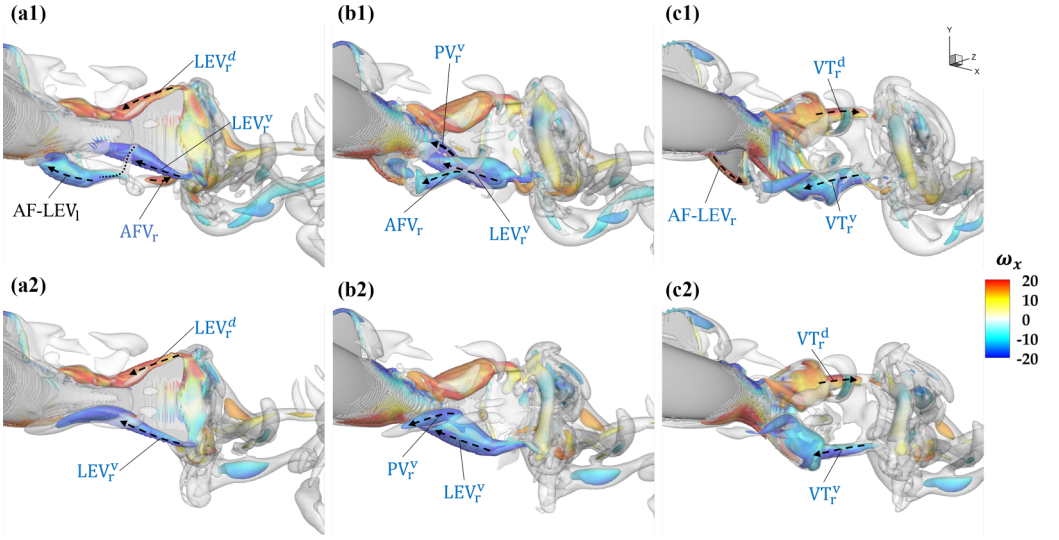

FIG. 7. Three-dimensional wake structures of (a1), (b1), and (c1) M1 and (a2), (b2), and (c2) M2 during the left-right stroke of the caudal fin at timesteps (a) $t/T = 0.063$, (b) $t/T = 0.25$, and (c) $t/T = 0.44$. The wake structures are visualized by the isosurface Q criterion, with $Q = 50$ (colored by streamwise vorticity contour) and $Q = 5$ (white).

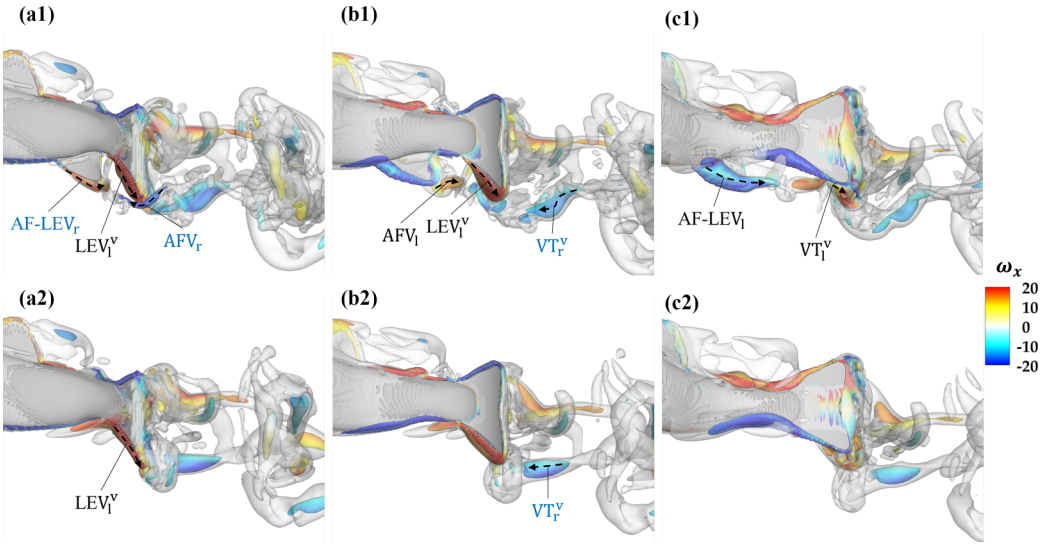

FIG. 8. Three-dimensional wake structures of (a1), (b1), and (c1) M1 and (a2), (b2), and (c2) M2 during the right-left stroke of the caudal fin at timesteps (a) $t/T = 0.63$, (b) $t/T = 0.87$, and (c) $t/T = 1.00$. The wake structures are visualized by the isosurface Q criterion, with $Q = 50$ (colored by streamwise vorticity contour) and $Q = 5$ (white).

are labeled with the abbreviation LEV, and LEVs formed on the AF are labeled with AF-LEV. Due to the complexity of vortex forming, shedding and interactions within an undulating cycle, subscripts l and r are used to differentiate between vortices that originate in the leftward and rightward strokes, following the convention set by Liu *et al.* [6] and Menzer *et al.* [49]. To visually aid this differentiation, text labels of vortices formed during the rightward stroke are also colored blue. Superscripts d and v are used to differentiate the LEVs and VTs formed on the dorsal and ventral sides of the fish.

The formation and shedding of LEV^d and the formation of VT$_r^d$ on the dorsal side of the fish body is largely similar between M1 and M2. Major differences are observed on the ventral side. In M1, AF-LEVs and AFVs are formed periodically on the leading edge and tip of the AF. Due to a heaving-pitching phase lead exhibited by the AF relative to the CF, AF-LEV formation precedes CF LEV formation. The timestep depicted in Fig. 7(a1) is during the rightward stroke, but the AF-LEV$_l$ is fully formed during the preceding leftward stroke. The formation and origin of AF-LEV$_l$ can be seen in Fig. 8(c1). Due to the proximity between the AF and CF, an extension of the AFV is absorbed by the LEV before the AFV is completely shed [Fig. 7(a1)]. At the timestep depicted in Figs. 7(b1) and 7(b2), relatively high C_T values are observed in Fig. 5(a) for CFs of both M1 and M2. Correspondingly, the LEV$_r^{v\prime}$s for both M1 and M2 are strong and coherent. The LEV of M2 is aided by the connected peduncle vortices (PVs), while the LEV of M1 is enhanced by a slightly weaker PV and the interaction with the AFV. In Fig. 7(b1) and 7(b2), the LEVs for both M1 and M2 start to separate, corresponding to the dip in $C_{T\,\mathrm{CF}}$ in Fig. 5(a).

The interaction of the CF with the shed AFV is depicted in Figs. 7(b1) and 8(c1). In M2, instead of an AFV, a PV is formed from the body shear layer in the absence of an AF. The PV then combines with the similarly oriented LEV at the root of the CF, as shown in Figs. 7(a2), 7(b2), and 7(c2). The AF in M1 diverts the body shear layer away from the body, leading to the formation of a AF-LEV [Fig. 7(a1)]. The AFV is formed through the combination of the AF-LEV and other AF-bound vortices and shear layers at the AF tip. The subsequently shed AFV then interacts with the CF at near the midchord point (chord defined as the length of the CF measured from the root at the

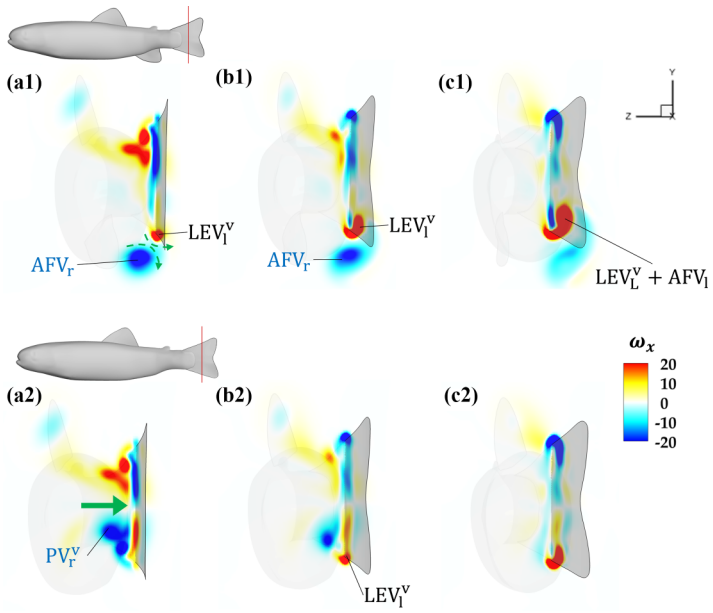

FIG. 9. Slice cut parallel to the yz plane made at the location denoted by the red line in M1 and M2 shown in lateral view above (a1) and (a2), showing the x vorticity ω_x for (a1)–(c1) M1 and (a2)–(c2) M2, at time steps (a1) and (a2) $t/T = 0.44$, (b1) and (b2) $t/T = 0.50$, and (c1) and (c2) $t/T = 0.56$. Green arrow indicating the direction of flow in a channel created by two closely set counterrotating vortices.

peduncle to the trailing edge), instead of the root, as shown in Fig. 7(b1). The similarly oriented AFV and LEV combine to become a larger and stronger VT to be shed at the tip of the ventral edge of the CF [Fig. 7(c1)].

The combining of LEV and AFV leads to a stronger VT than the combining of PV and LEV. At the same time, the AF-LEV$_r$ forms and leads to the shedding of the AFV$_l$, to interact with the LEV$_l$. The development of the VT$_r^v$ following a similar formation process during the leftward stroke can be observed in Fig. 8 for both M1 and M2. The AFV$_r$ in M1 helps support and elongate the similarly oriented VT$_r^v$, so that it stays coherent until the end of the cycle. The PV$_r^v$ that continuously feeds into the LEV^v enhances the VT$_r^v$ in M2 in a similar manner. However, the strength and speed of the PV$_r^v$ seems insufficient to support the VT$_r^v$ for long durations, as demonstrated by the comparatively shorter VT$_r^v$ in Fig. 8(b2) than in Fig. 8(b1). In contrast, the AFV stays at least partially connected with the VT^v for the entirety of the leftward half cycle.

Timesteps shown in Figs. 7(c) and 11(a) correspond to instances of large CF C_T difference between M1 and M2. The vortices shed by the AF at these timesteps in M1, in addition to feeding into the VT, also skirt along the ventral-side leading edge of the CF. To further examine the mechanism through which the capturing of the AFV enhances thrust produced by the CF, for timesteps of large $C_{T\,\mathrm{CF}}$ difference between M1 and M2, a slice cut is made to show the x-direction vortex strength in Fig. 9, near the location where the CF intercepts the AFVs. The time sequence selected here demonstrates that the dominant mechanism through which the AFV enhances the LEV$_l^v$ is by helping its initiation. During this time, the CF undergoes a reversal of the flapping direction. The AFV produced during the rightward stroke rotates in the negative x direction, the same as the PV generated in M2. Whereas the PV is located near the midspan location of the CF, the AFV is underneath the leading edge of the CF, an opportune placement because the shearing between the vortex and the CF leading edge causes a positive LEV$_l^v$ to form more readily than M2. In Fig. 9(a2), the LEV of M2 is absent due to the CF being in a transitional stage and having a low

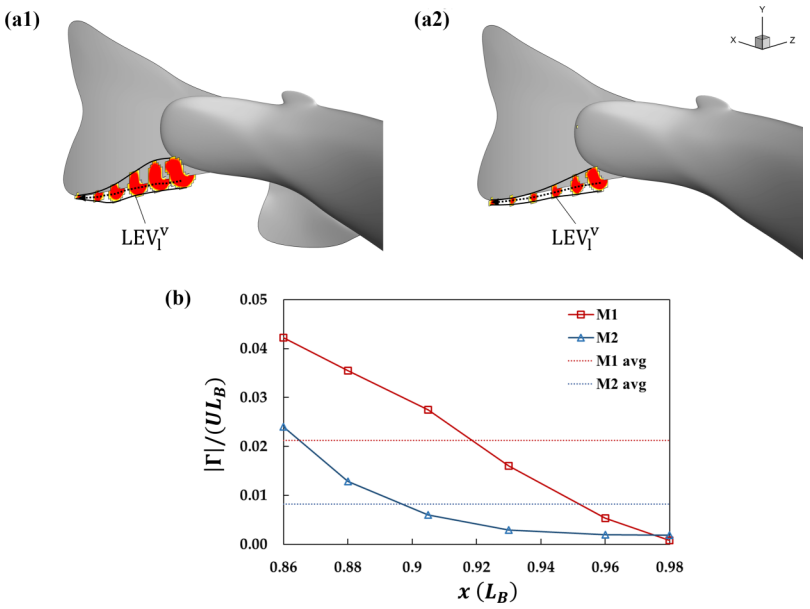

FIG. 10. At time step $t/T = 0.50$, six equally spaced x slices made on the caudal fin (CF) from near the root ($x = 0.86L_B$ from the snout of the trout) to near the tip ($x = 0.98L_B$), showing dominant vortex formations on (a1) M1 and (a2) M2, with the cores traced by directional dotted lines also indicating the direction of rotation, the solid black lines denoting the boundaries of leading-edge vortices (LEVs). The strengths of the LEVs on the slices are plotted in (b).

angle of incidence in the flow; the LEV of M1 is already formed due to the shearing from the AFV. In subsequent timesteps, the LEV continues to grow in M1 and starts to form in M2, the result being a consistently stronger LEV in the presence of an AFV during the stroke-reversal stage, as seen in Figs. 9(a1)–9(c1) compared with Figs. 9(a2)–9(c2).

A less measurable benefit of the AFV, made apparent also by Fig. 9, is the avoidance of lateral jet formations due to channels existing between closely placed counterrotating vortices, as denoted in Figs. 9(a2). As mentioned before, the AF diverts the body shear layer away ventrally, as those vortices shed can more directly benefit the CF leading edge, whereas in its absence, vortices travel in toward the midspan region of the CF. Dorsal and ventral PVs congregate midspan of the CF to produce a channel between them, producing a laterally facing jet, labeled by a green arrow in Fig. 9(a2). Though lateral jets are beneficial in maneuverability [29], when rectilinear propulsion is the goal, energy is wasted. The lateral jet in Fig. 9(a2) can also resist the leftward translation of the CF, accounting for further energy expenditure. By diverting vortices to the outer edges of the CF, this energy waste is avoided.

To quantify the benefit of the AFV-LEV interaction described in Fig. 9 and ensure that it is not limited to the region near the slice cut, a series of equally spaced slices are made along the entire CF leading edge at the time of stroke reversal and large CF thrust enhancement to show the core of the LEV$_1^V$, and the circulation strength of the core is calculated at the slice-cut locations. Figures 10(a1)–10(a2) show slices displaying ω_x contours with a cutoff value near the upper limit of the contour legend range shown in Fig. 9 to exclude auxiliary vortices and focus on only the core of the LEV$_1^V$. In Fig. 10(b), the circulation strength ($|\Gamma|$) is nondimensionalized by the product of free-stream velocity (U_∞) and L_B. The LEV cores of M1 are larger than those of M2 along the whole CF leading edge. The circulation plot shown in Fig. 10(b) confirms this visual observation, as the circulation strength at each station except the tip-bound one is higher in M1 than in M2. The difference is especially large near the middle of the space between the

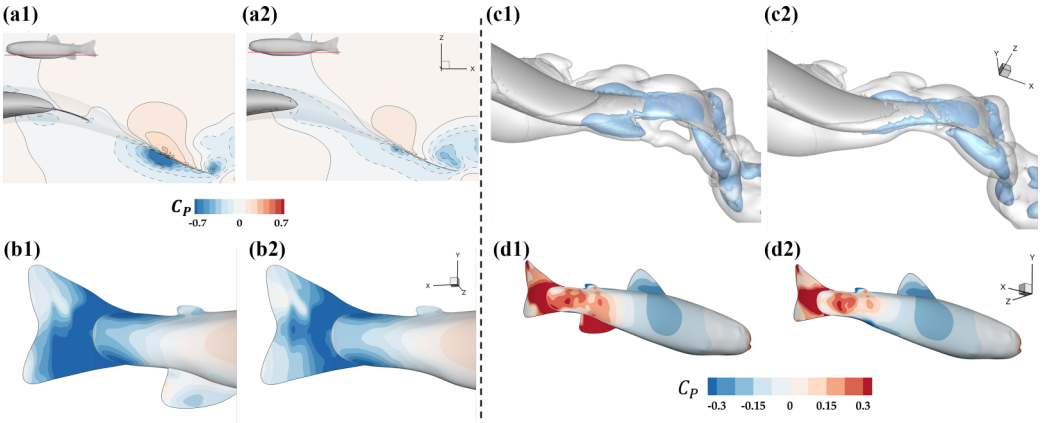

FIG. 11. Pressure plots at (a) and (b) $t/T = 0.50$ and (c) and (d) $t/T = 0.88$, with (a) a slice cut through the lower body, the precise position denoted in (a1) and (a2) top-left corner with a red line, and dashed contour lines separating regions with negative pressure, (b) surface pressure on the suction side of the peduncle-caudal fin (CF) section, (c) pressure isosurface with $C_P = -0.20$ (blue) and $C_P = -0.05$ (white), and (d) surface pressure contour of the whole right side of the fish body on (a1), (b1), and (c1) M1 and (a2), (b2), and (c2) M2.

root and the tip. Whereas the LEV circulation plot for M2 exhibits a quadratic pattern, whereby it is the strongest at the root and quickly drops off and levels out as we move further downstream, the LEV circulation plot for M1 exhibits a more linear pattern; the decreasing of the LEV circulation as the station is moved nearer the tip is less drastic. In this timestep, both $\mathrm{LEV}_{\mathrm{l}}^{\mathrm{v}}$ initiation due to the $\mathrm{AFV}_{\mathrm{r}}$ and absorption of $\mathrm{AF\text{-}LEV}_{\mathrm{l}}$ extension by the $\mathrm{LEV}_{\mathrm{l}}^{\mathrm{v}}$ are in effect at different locations, causing a uniform circulation enhancement along the entirety of the CF leading edge.

Next, to get from fluid physics back to forces on the body, pressure contours are depicted on a slice cut, the position of which is shown in Figs. 11(a1) and 11(a2), top-left corner, intersecting part of the TK, the AF, and a quarter-span of the CF. The timestep shown in Figs. 11(a) and 11(b), $t/T = 0.50$, corresponds to the instant where large thrust enhancement is observed in Fig. 5(a). The pressure contour shown on the y slice shows that the two opposite sides of the CF are dominated by contrasting pressure-suction pressure fields; the region to the left of the CF is predominantly positive (pressure), while the left side is predominantly negative (suction). Due to the orientation of the CF, the pressure and suction sides lean downstream and upstream of the CF, a configuration conducive to thrust production. Following the trajectories of the contour lines separating positive and negative pressure regions in Figs. 11(a1) and 11(a2), one observes that more leaching of the suction region occurs in M2 due to the tendency of fluid to flow from a high-pressure region to regions of negative pressure, reducing the overall pressure gradient. In contrast, the AF in M1 can preserve the pressure gradient better by preventing the crossflow of fluid from the positive- to negative-pressure side of the body, leading to the stronger and more expansive suction region in M1 compared with M2. The overall result is a larger lateral pressure gradient across the CF of M1, leading to more forward thrust produced by the CF in M1 than in M2. The CF surface pressure contours of M1 and M2, depicted in Figs. 11(b1) and 11(b2), show that the comparative expansiveness of the region with high suction force in M1 is not limited to the leading edge of the CF but also extends to much of the ventral surface of the CF. Due to the orientation of the CF, the larger high-suction region on the CF surface in M1 than M2 also contributes to higher forward thrust force. The trajectory of contour lines separating negative and positive pressure regions in Figs. 11(a1) and 11(a2) also suggests the other functions of the AF, in reducing body drag and producing AF thrust, as the downstream side of the AF and TK in M1 is consistently positive in pressure, whereas the negative pressure resides downstream of the TK in M2.

TABLE II. Summary of hydrodynamic performance: cycle-average coefficient of thrust.

d/d_0	0.75	1.0	1.25	1.50
TK $\bar{C}_T$	−0.236	−0.234	−0.246	−0.269
AF $\bar{C}_T$	0.0475	0.0267	0.00955	−0.00150
CF $\bar{C}_T$	0.444	0.482	0.501	0.491

To further illustrate body-drag reduction and AF thrust production, pressure isosurface and full-body surface pressure contour for both M1 and M2 are shown in Figs. 11(c) and 11(d) for the timestep $t/T = 0.88$, when a large difference in body drag and nonnegative AF thrust is observed in Fig. 5(a). The upstream surface of the peduncle region is predominantly negative pressure in both M1 and M2, but the AF in M1 can extend the negative-pressure region a bit further forward and enhance the bottom edge of that region, as seen by the more coherent negative-pressure isosurface in Fig. 11(c1). The high suction force upstream of the TK and AF helps reduce drag on those body parts. In the body surface contour [Figs. 11(d1) and 11(d2)], on the other side of the body, though the anterior portion looks similar, the pressure side of the posterior region is stronger and more expansive in M1 than in M2. Whereas the high-pressure force is limited to near the middle of the right-side surface of the fish in M2, with the suction force creeping over from the other side at the ventral edge, in M1, the high-pressure region extends from the dorsal to the ventral edge of the entirety of the posterior surface. This is also due to the lack of lateral crossflow due to the obstruction provided by the AF. The downstream side of the AF is also dominated by high pressure, leading to thrust production by the AF.

B. Effect of AF-CF spacing

Different fish species and trout individuals may exhibit body shapes and morphologies differing from the ones of the individual used for analysis thus far. This section explores the dependence of vortex-fin interaction on the spacing between the AF and CF. With the definition of d shown in Fig. 2(b1) and d_0 denoting the AF-CF spacing in the baseline model, cases are run with d/d_0 varying from 0.75 to 1.50, and comparisons are made to the baseline case (M1) of $d/d_0 = 1$. The analysis in this section will focus on body parts most affected by the AF, including the AF itself, the CF, and the TK. The cycle-average thrust coefficient $\bar{C}_T$ of different body parts in different cases is summarized in Table II. The trend of $\bar{C}_T$ as d/d_0 changes is shown in Fig. 12(b). In Zhang *et al.* [25], the optimal range of spacing and relative heaving phase between tuna-inspired median fins and

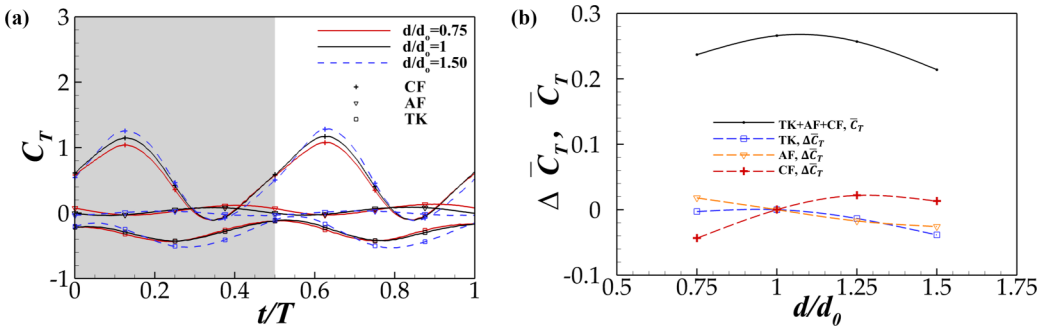

FIG. 12. (a) Time history of instantaneous C_T over a typical cycle for varying anal fin (AF)-caudal fin (CF) spacing. (b) Performance trend in terms of cycle-averaged coefficient of thrust ($\bar{C}_T$) for the sum of body parts and deviation from baseline case ($\Delta\bar{C}_T = \bar{C}_T - \bar{C}_{T_{M1}}$) for individual body parts with respect to AF-CF spacing d/d_0.

CFs that induced desirable vortex interaction was found to encompass the configuration of a real tuna. Similarly, the performance peak in this paper is found at $d/d_0 = 1$, indicating the original, anatomically realistic configuration on the biological fish as optimal for forward propulsion. The AF position of the fish induces this optimum by striking a balance between thrust enhancement and drag reduction. The instantaneous C_T for the TK, AF, and CF over a full cycle, shown in Fig. 12(a), reveals that all three body parts are affected by the changing position of the AF. As AF-CF spacing is decreased, with the AF moving more posterior, the AF thrust production is expected to increase due to the posterior body having a larger undulation amplitude, as determined by the undulation envelope of the fish, leading to larger pitching-heaving amplitudes for the AF. The simulation result shown in Fig. 12(a), with the $C_{T\,\mathrm{AF}}$ line of $d/d_0 = 0.75$ being overall higher than that of $d/d_0 = 1.0$, agrees with expectations.

For the TK drag, significant variation from baseline is observed in the $d/d_0 = 1.50$ configuration, with the AF being more anterior. Although slightly less drag inducing at the beginning of a stroke (half cycle), for most of a stroke, in $t/T = (0.15,\ 0.5)$ and $(0.65,\ 1.0)$, the TK in the $d/d_0 = 1.50$ configuration produces more drag than in the baseline case. From the $\bar{C}_T$ summary shown in Table II, it can be calculated that the TK drag is increased by 15.0% by changing d/d_0 from 1.0 to 1.50 and 0.85% by changing d/d_0 from 1.0 to 0.75. The original positioning of the AF provides more significant TK drag reduction than a more anteriorly positioned AF (larger d/d_0), and further decrease of AF-CF does not provide significant additional TK drag reduction. For the CF, the most drastic difference in instantaneous C_T between configurations with an anterior AF (large d/d_0) and a posterior AF (small d/d_0) occurs at the peaks of thrust production, when $t/T = 0.13$ during the rightward stroke and $t/T = 0.63$ during the leftward stroke. A more anteriorly placed AF brings about higher peak CF C_T, with a clear separation among cases with d/d_0 values of 1.50, 1.0, and 0.75. A less significant difference is observed during stroke reversal, like the difference between the CF C_T curves of M1 and M2, most representatively at $t/T = 0.44$, with a trend that is the opposite of the thrust enhancement at CF C_T peaks. The largest improvement from baseline in CF $\bar{C}_T$ is achieved with $d/d_0 = 1.25$. The cycle-averaged CF thrust coefficient $\bar{C}_{T_{\mathrm{CF}}}$ is 0.501 for $d/d_0 = 1.25$ and 0.482 for $d/d_0 = 1.00$, resulting in an overall improvement of 3.9% CF thrust, benefiting from thrust enhancements both in stroke reversal and at the peaks of thrust production. The difference occurring at the thrust reversal observed in Fig. 12(a) is likely the result of the same vortex interaction causing the difference in CF thrust production between M1 and M2 observed in Fig. 5(a), examined in Sec. III A. Next, the flow physics causing significant variations in TK drag reduction and CF thrust enhancement during a stroke are examined separately.

To explain the reduction of TK drag due to moving the AF more anterior from a fluid physics standpoint, pressure isosurfaces in flow around the fish and pressure contour on the surface of the body of the fish are plotted in Fig. 13 for cases with posterior-most ($d/d_0 = 0.75$) and anterior-most ($d/d_0 = 1.50$) AFs. Extreme cases are chosen for comparison to highlight the flow phenomenon. The pressure on and around the DF and the anterior half of the fish TK are unaffected by the varying position of the AF. In the posterior region, near the peduncle, the AF helps maintain and expand the suction region on the upstream side. A comparison of pressure isosurfaces shown in Figs. 13(a1) and 13(a2) elucidates the expansion and improved coherence of the suction region in the fluid ahead of the peduncle. The surface pressure contour in this region on the pressure side also shows an expansion and more coherence of regions of desirable pressure force due to a more posterior AF. Whereas in the $d/d_0 = 1.50$ configuration the bottom of the peduncle shows an extension of the negative pressure from the suction side and a reduction of the desirable positive pressure region, the peduncle in the $d/d_0 = 0.75$ configuration has positive pressure residing across the entirety of the surface on the right side. Overall, the benefit of a more posterior AF in terms of TK drag reduction is in preventing crossflow that can occur due to the narrowing of the TK shape at the peduncle region, thus maintaining the beneficial pressure gradient across the peduncle.

The added benefit of a more posterior AF, that of high thrust production by the AF itself, can also be explained here. The pressure isosurface on the AF shows a more coherent suction region on the leading edge of the further upstream side of the AF. This indicates not only a stronger

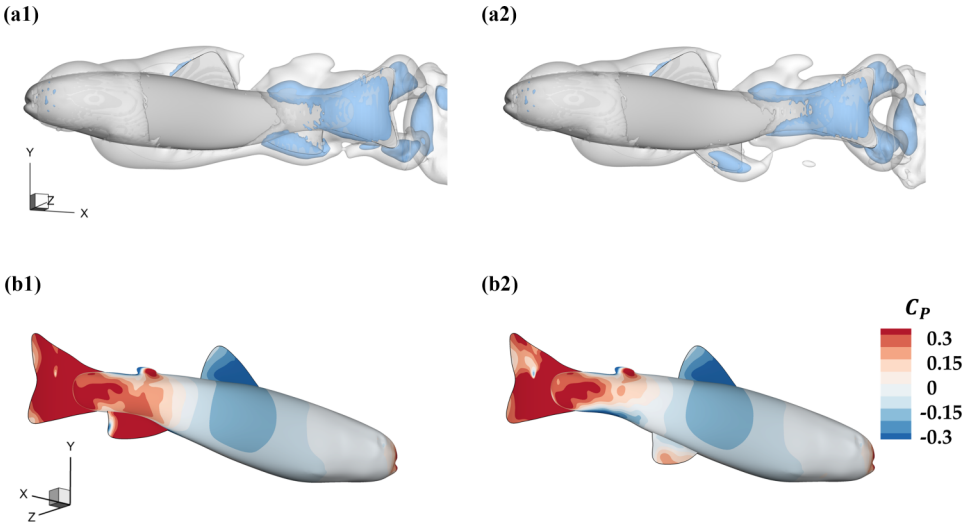

FIG. 13. (a) Pressure isosurface at $t/T = 0.88$, with $C_P = -0.05$ (white, transparent) and $C_P = -0.20$ (blue), (b) pressure contour on fish body at the same time step, for (a1) and (b1) $d/d_0 = 0.75$ and (a2) and (b2) $d/d_0 = 1.50$.

forward-pointing suction force but also a stronger AF-LEV, both leading to higher $C_{T\,\mathrm{AF}}$ observed in Fig. 12(a) at the instant depicted in Fig. 13. The surface pressure contour on the downstream side of the AF in the more posterior case also shows an expansion and enhancement of positive pressure on the AF.

Next, we examine the effect of AF placement on the CF thrust production and explain variations in the CF C_T curve seen in Fig. 12(a) from a flow physics standpoint. The interactions of AF- and CF-bound vortices at a timestep of significant difference in instantaneous CF C_T are depicted in Fig. 14 for the extreme cases. Like M1 shown in Figs. 7 and 8, AFVs form around the AF and are shed periodically during flapping in all the AF locations tested. When the AF and CF are positioned close to each other, such as in the configuration shown in Fig. 14(a), the flapping phases of the AF and CF are also similar, so that the production of the AF-LEV and LEV would be close to synchronous. In comparison, with a larger d/d_0, as shown in Fig. 14(b), though the same coherent and attached LEV tubes can be seen on the leading edge of the CF, no AF-LEV can be clearly identified. Instead, a detached AFV has been shed from the AF and advected downstream. Ample

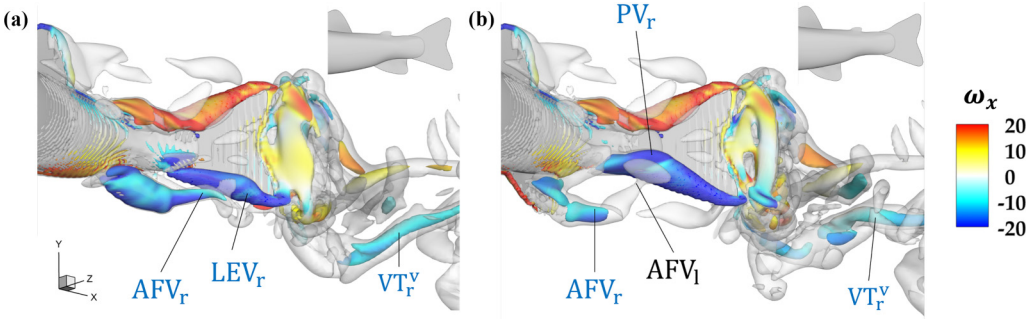

FIG. 14. Three-dimensional wake structure visualized by the isosurface Q criterion, with $Q = 50$, colored by streamwise vorticity (ω_x) contour, and $Q = 5$ (white) for (a) $d/d_0 = 0.75$. (b) $d/d_0 = 1.50$, at $t/T = 0.13$.

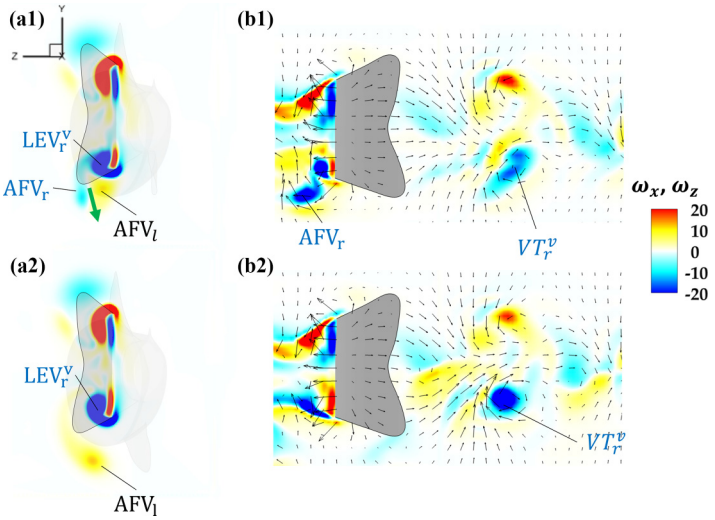

FIG. 15. (a) and (b) ω_x and ω_z showing on the slicecut made at the same location as in Figs. 9, 6(c), and 6(d) at $t/T = 0.13$. (a1) and (b1) $d/d_0 = 0.75$. (a2) and (b2) $d/d_0 = 1.50$.

spacing between the AF and CF in the $d/d_0 = 1.50$ case allows for the full development of the PV, amplifying the LEV at the CF root through their connection. In contrast, in the $d/d_0 = 0.75$ case, the AF is placed in the narrowing peduncle, interrupting the formation of the PV. The shed AFV in the $d/d_0 = 0.75$ case runs parallel with the CF without interception and does not enhance the similarly rotating LEV.

The flow around the narrowing, streamlined peduncle causes the AFV to be advected up toward the CF in the $d/d_0 = 1.50$ case. The subsequent constructive interaction between the AFV and CF LEV is next examined. As shown in Figs. 14(b) and 15(a2), in the $d/d_0 = 1.50$ case, the LEV generated during the rightward stroke interacts with the AFV originating in the leftward stroke. As a result, the $\mathrm{AFV_l}$ rotates counter to the $\mathrm{LEV_r}$ and stabilizes it at the peak of thrust production. At the same timestep, in the $d/d_0 = 0.75$ case, both $\mathrm{AFV_l}$ and $\mathrm{AFV_r}$ affect the formation of the $\mathrm{LEV_r}$, as shown in Fig. 15(a1). Consistent with the observation from Fig. 14(a), the cores of the $\mathrm{AFV_r}$ and $\mathrm{LEV_r}$ remain separate. The close proximity between the counterrotating $\mathrm{AFV_l}$ and $\mathrm{AFV_r}$ cores facilitate a jet forming between them, pointing downward, and destabilizing the $\mathrm{LEV_r}$ by pulling it away from the CF. The strong and stable $\mathrm{LEV_r}$ in the $d/d_0 = 1.50$ case eventually forms a strong VT to have a lasting effect even as it is shed downstream. A narrowing of the space between the VTs is observed in Fig. 14(b), with the $\mathrm{VT_r^v}$ moved up closer to the VT from the dorsal side, toward the left end of the tubes. The proximity of counterrotating vortices can be more stable and generate a stronger and more concentrated jet between them. Figures 15(b1) and 15(b2) confirm that the core of the $\mathrm{VT_r^v}$ is indeed stronger for $d/d_0 = 1.50$ than for $d/d_0 = 0.75$, due to PV enhancement and AFV stabilization of the LEV in the anterior-AF case. With little difference in the VT from the dorsal side, the combined effect of the $\mathrm{VT_r^v}$ being stronger and closer to the body midline is a stronger jet, as indicated by the field of vectors with large amplitudes in the space between the two VTs.

More desirable AF-CF interaction occurring when the distance between the two fins is increased is a surprising finding. However, a justification can be found by considering the phase difference between the AF and CF. For this, we need to not only consider the flapping phase difference between the two fins, but also, the finite and varying distance between the fins determines that the vortex capturing is also phase shifted. In other words, the vortex shed from the AF tip takes a finite time to reach the CF, and by then the CF flapping phase would have changed from the time when the AFV

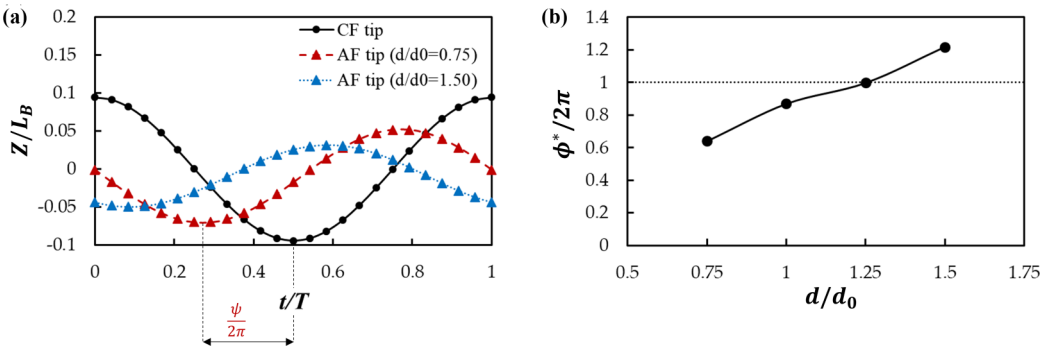

FIG. 16. Relative flapping motion of the anal fin (AF) and caudal fin (CF) at different locations. (a) Lateral excursion of the CF and AF tips was tracked for an entire cycle, showing cases of the maximum and minimum AF-CF spacings for AF. (b) Global phase difference between AF and CF for different AF-CF spacing cases.

is shed. This phase shift due to the time it takes for the AFV to travel from the AF to the CF needs to be considered. A glance at Fig. 16(a) reveals that the flapping phase (in terms of lateral excursion of the fin tips) increases as the AF is moved further away from the CF; the posterior AF has a curve closer in phase with the CF tip, while the anterior-most AF has a curve more shifted in phase compared with the CF tip. Then we borrow the global phase (ϕ^*) definition developed by Kinsey and Dumas [18]. A variation of this phase definition has been used by Ribeiro *et al.* [15] to extract a coherent trend in the wake-foil interaction of tandem flapping foils. In this definition, the distance the vortex has to travel is defined by the x distance between the AF and CF tips ($x_{\mathrm{CF_{tip}}} - x_{\mathrm{AF_{tip}}}$) and normalized by the convection speed of the vortex, approximated as the incoming flow speed U_∞ and the flapping period T. The Greek letter ψ is used to represent the flapping phase, the phase difference in lateral excursions of the CF and AF tips [Fig. 16(a)] between the AF and the CF. Then the global phase ϕ^* is defined by Eq. (6)

$$\phi^* = 2\pi \frac{x_{\mathrm{CF_{tip}}} - x_{\mathrm{AF_{tip}}}}{U_\infty T} + \psi. \tag{6}$$

The resulting global phases of the four AF-CF spacing-varying cases are shown in Fig. 16(b). This trend corresponds well with the general trend of increasing the peak thrust coefficient $C_{T_{\mathrm{max}}}$ as d/d_0 increases, shown in Fig. 12(a). The value of ϕ^* of the $d/d_0 = 1.25$ case being close to 2π ($0.997 \times 2\pi$) indicates a good synchronization in this case between the shedding of the AFV and the capturing of it by the CF, corresponding well with the observation that CF C_T reaches a peak when $d/d_0 = 1.25$ in Fig. 12(b).

With the effects of the AF on TK drag force reduction and CF thrust force generation explored and AF auxiliary thrust production considered, summing all these effects together, the original position of the AF is found to be the most conducive to forward propulsion, as shown in Fig. 12(b).

C. Effect of varying AF height

By varying the height of the AF, while keeping the leading-edge arc length l_{AF} constant, the opening and closing of the AF are mimicked. Knowledge from this section can provide a better understanding of the reason behind the spontaneous opening and closing of the AF of the fish and inform the design of a hydrodynamically optimal underwater vehicle. The extreme cases tested in this paper have AF heights b_{AF} of $0.75b_{\mathrm{AF_0}}$ and $1.25b_{\mathrm{AF_0}}$, where $b_{\mathrm{AF_0}}$ is the height of the AF in the anatomically accurate model (M1). AFs with varying heights are shown in Fig. 2(b3). As a result of varying fin height, the surface area of the fin is also varied, corresponding well with observation in real fish [29]. The surface area variation is approximately proportional to variations

TABLE III. Performance summary of varying AF height, showing the cycle-average values of coefficient of thrust, coefficient of power, and for the propulsors (AF and CF), the propulsive efficiency, calculated as the ratio of $\bar{C}_T/\bar{C}_{\mathrm{PW}}$.

	$b_{\mathrm{AF}}/b_{\mathrm{AF}_0}$	$\bar{C}_T$	$\bar{C}_{\mathrm{PW}}$	η
TK	0.75	−0.240	0.921	
	1.00	−0.234	0.932	
	1.25	−0.232	0.939	
AF	0.75	0.0181	0.0660	27.4%
	1.00	0.0268	0.0908	29.5%
	1.25	0.0334	0.115	29.0%
CF	0.75	0.468	0.855	54.7%
	1.00	0.482	0.865	55.7%
	1.25	0.489	0.869	56.3%
Sum	0.75	0.246	1.842	
	1.00	0.275	1.888	
	1.25	0.290	1.923	

in b_{AF}, with the largest AF surface area $S_{\mathrm{AF}} = 1.13S_{\mathrm{AF}_0}$ corresponding to $b_{\mathrm{AF}} = 1.25b_{\mathrm{AF}_0}$ and the smallest $S_{\mathrm{AF}} = 0.75S_{\mathrm{AF}_0}$ corresponding to $b_{\mathrm{AF}} = 0.75b_{\mathrm{AF}_0}$. The scaling proportionality between AF height and surface area when reducing the AF size corresponds well with the observation that the leading-edge arc remains the same shape and overall angle relative to the ventral edge of the TK in Fig. 2(b3). The changing of leading-edge arc shape and overall angle when increasing the size of the AF while keeping the arc length constant leads to the loss of scaling proportionality between AF height and surface area. The ARs calculated using $\mathrm{AR} = b_{\mathrm{AF}}^2/S_{\mathrm{AF}}$ for the cases of $b_{\mathrm{AF}}/b_{\mathrm{AF}_0} = 0.75$, 1.0, and 1.25 are 0.86, 0.62, and 0.45, respectively.

The performance of the TK and fins affected by the varying AF size is summarized in Table III. Increasing AF size leads to increased $\bar{C}_T$ in both the AF and CF. Recalling that the coefficient of thrust is calculated uniformly for all body parts using the surface area of the CF, an increase in AF $\bar{C}_T$ directly corresponds to increase in thrust force. This is expected and discussed by Standen and Lauder [29] due to an increase in surface area. The TK and CF also receive benefits from increased AF height, as seen by the increase of $\bar{C}_T$ on both TK and CF rows, as $b_{\mathrm{AF}}/b_{\mathrm{AF}_0}$ increases. However, on the TK, AF, and CF, the increase of $\bar{C}_T$ from $b_{\mathrm{AF}}/b_{\mathrm{AF}_0} = 0.75$ to $b_{\mathrm{AF}}/b_{\mathrm{AF}_0} = 1.00$ is more drastic than the increase of $\bar{C}_T$ from $b_{\mathrm{AF}}/b_{\mathrm{AF}_0} = 1.00$ to $b_{\mathrm{AF}}/b_{\mathrm{AF}_0} = 1.25$, indicating a plateau in the hydrodynamic force trend; though significant benefit is gained by opening the AF from a relatively closed position ($b_{\mathrm{AF}}/b_{\mathrm{AF}_0} = 0.75$) to the position exhibited by the model fish ($b_{\mathrm{AF}}/b_{\mathrm{AF}_0} = 1.00$), further opening of the AF rays by the same proportion (to $b_{\mathrm{AF}}/b_{\mathrm{AF}_0} = 1.25$) does not yield significant gains.

Increased surface area can also lead to a higher power requirement, as confirmed by the comparison of $\bar{C}_{\mathrm{PW}}$ in Table III for the TK, AF, and CF. The largest variation is observed on the AF. A 27.3% decrease and 26.6% increase in AF $\bar{C}_{\mathrm{PW}}$ is observed when AF height is reduced and increased by 25%, respectively. Propulsive efficiency (η) is calculated as $\eta = \bar{C}_T/\bar{C}_{\mathrm{PW}}$, and it is optimized in the original, anatomically accurate model, whose $b_{\mathrm{AF}}/b_{\mathrm{AF}_0} = 1.00$. For the CF, steady increases of η are observed as b_{AF} is increased, though the increases are slight ($\sim$1% variation), and a plateau seems to approach. Overall, summing the effect of both propulsors, a performance peak exists in $b_{\mathrm{AF}} \in (0.75,\ 1.25)b_{\mathrm{AF}_0}$, near the anatomically accurate configuration.

IV. CONCLUSIONS

In this paper, we explored the interaction of the AF of a fish with other body parts, focusing on the vortex-fin interaction between the AF and CF. It is found that the LEV formed on the CF aids

in thrust production by (1) creating a forward-pointing suction force, and (2) when shed, forming counterrotating VTs that enhance the backward-facing jet in the channel between the tubes. The AF is found to produce coherent LEVs that are separate from body vortices, and the thrust-type vortices shed from the AF also enhance the thrust production of the CF. The AFV from the AF encounters the leading edge of the CF during stroke reversal to help initiate and stabilize the CF LEV through the shearing between the AFV and the CF surface. In the presence of the AF, the CF can produce stronger and longer-lasting ventral VTs that are closer to the dorsal VTs of the same cycle, resulting in a stronger and more focused backward-facing jet. An 8.6% enhancement of the CF thrust is achieved in the presence of the AF. Through parametric studies, it is also revealed that, by adjusting for the wake-capture phase difference between the AF and CF, the AFV can also stabilize the CF LEV in the middle of a tail stroke, resulting in enhancement of lift-based thrust production at the peaks of CF thrust generation. Combining both mechanisms, the AF at the optimal position provides an additional enhancement of CF thrust compared with the baseline case.

Additional functions of the AF are found to include a reduction of TK drag and a small amount of thrust production. In the baseline case, a 18.6% decrease in TK drag is attributed to the AF blocking lateral crossflow and the loss of pressure gradient. The AF is also found to produce 5.3% of the total propulsive force in its original size and position. By adjusting the position of the AF along the fish TK, different amounts of reduction in TK drag and production of the AF thrust are found, with a more posterior AF producing more thrust while maintaining TK drag reduction and a more anterior AF producing less thrust and less effective in reducing TK drag. This, combined with the diminishment of CF thrust enhancement by an AF extremely close to the CF, due to vortex capturing phase shifts, the optimal position of the AF is the original, anatomically accurate configuration, wherein the net forward force of the full fish body is the highest. Similarly, by varying the height and shape of the AF to mimic its opening and closing, it is also found that the original anatomically accurate configuration is optimal for propulsive efficiency, defined as the ratio of the cycle-average coefficient of thrust and cycle-average coefficient of power.

The biological height and surface area of the AF of the fish is found to be optimal for forward propulsive efficiency in steady rectilinear swimming compared with other AF configurations via mechanisms elucidated in this paper. However, the role of the AF in maintaining lateral-directional stability and the ability of trout to actively control the AF in coordination with the DF, paired fins, and TK remain interesting areas for future studies.

ACKNOWLEDGMENTS

Thanks to members of the Lauder Lab for assistance with fish care and with the trout kinematic and hydrodynamic experiments and especially to Dr. Robin Thandickal for his insights and assistance with calculating and interpreting pressure on fish and robot body surfaces. Additionally, thanks to the University of Virginia Research Computing Group for the availability of the Rivanna supercomputing cluster. This paper was supported by grants from the Office of Naval Research (No. N00014-14-1-0533 and No. N00014-15-1-2234) and National Science Foundation (No. 093088-17158 to G.V. Lauder and No. CNS-1931929 to H. Dong).

[1] J. M. Anderson, K. Streitlien, D. S. Barrett, and M. S. Triantafyllou, Oscillating foils of high propulsive efficiency, J. Fluid Mech. **360**, 41 (1998).

[2] M. J. Lighthill, Aquatic animal propulsion of high hydromechanical efficiency, J. Fluid Mech. **44**, 265 (1970).

[3] M. S. Triantafyllou, G. S. Triantafyllou, and D. K. P. Yue, Hydrodynamics of fishlike swimming, Annu. Rev. Fluid Mech. **32**, 33 (2000).

[4] J. D. Eldredge and A. R. Jones, Leading-edge vortices: Mechanics and modeling, Annu. Rev. Fluid Mech **51**, 75 (2019).
[5] G. Liu, H. Dong, and C. Li, Vortex dynamics and new lift enhancement mechanism of wing-body interaction in insect forward flight, J. Fluid Mech. **795**, 634 (2016).
[6] G. Liu, Y. Ren, H. Dong, O. Akanyeti, J. C. Liao, and G. V. Lauder, Computational analysis of vortex dynamics and performance enhancement due to body-fin and fin-fin interactions in fish-like locomotion, J. Fluid Mech. **829**, 65 (2017).
[7] I. Borazjani and M. Daghooghi, The fish tail motion forms an attached leading edge vortex, Proc. R. Soc. B **280**, 20122071 (2013).
[8] T. Y. Wu, Fish swimming and bird/insect flight, Annu. Rev. Fluid Mech. **43**, 25 (2011).
[9] R. R. Harbig, J. Sheridan, and M. C. Thompson, The role of advance ratio and aspect ratio in determining leading-edge vortex stability for flapping flight, J. Fluid Mech. **751**, 71 (2014).
[10] C. Li, H. Dong, and K. Zhao, A balance between aerodynamic and olfactory performance during flight in drosophila, Nat. Commun. **9**, 3215 (2018).
[11] H. Dong and Z. Liang, Effects of ipsilateral wing-wing interactions on aerodynamic performance of flapping wings, in *Proceedings of the 48th AIAA Aerospace Sciences Meeting Including the New Horizons Forum and Aerospace Exposition* (American Institute of Aeronautics and Astronautics, Orlando, Florida, 2010).
[12] J. C. Liao, D. N. Beal, G. V. Lauder, and M. S. Triantafyllou, Fish exploiting vortices decrease muscle activity, Science **302**, 1566 (2003).
[13] J. C. Liao, D. N. Beal, G. V. Lauder, and M. S. Triantafyllou, The Kármán gait: Novel body kinematics of rainbow trout swimming in a vortex street, J. Exp. Biol. **206**, 1059 (2003).
[14] L. Kang, W. Cui, X.-Y. Lu, and H. Huang, Hydrodynamic force induced by vortex-body interactions in orderly formations of flapping tandem flexible plates, Phys. Fluids **34**, 021901 (2022).
[15] B. L. R. Ribeiro, Y. Su, Q. Guillaumin, K. S. Breuer, and J. A. Franck, Wake-foil interactions and energy harvesting efficiency in tandem oscillating foils, Phys. Rev. Fluids **6**, 074703 (2021).
[16] I. Akhtar, R. Mittal, G. V. Lauder, and E. G. Drucker, Hydrodynamics of a biologically inspired tandem flapping foil configuration, Theor. Comput. Fluid Dyn. **21**, 155 (2007).
[17] X. Shao, D. Pan, J. Deng, and Z. Yu, Hydrodynamic performance of a fishlike undulating foil in the wake of a cylinder, Phys. Fluids **22**, 111903 (2010).
[18] T. Kinsey and G. Dumas, Optimal tandem configuration for oscillating-foils hydrokinetic turbine, J. Fluids Eng. **134**, 031103 (2012).
[19] P. Han, Y. Pan, G. Liu, and H. Dong, Propulsive performance and vortex wakes of multiple tandem foils pitching in-line, J. Fluids Struct. **108**, 103422 (2022).
[20] A. S. Hegde, P. S. Gurugubelli, and V. Joshi, Effect of combined heaving and pitching on propulsion of single and tandem flapping foils, arXiv:2202.06550v2.
[21] D. Rival, G. Hass, and C. Tropea, Recovery of energy from leading- and trailing-edge vortices in tandem-airfoil configurations, J. Aircr. **48**, 203 (2011).
[22] M. S. Triantafyllou, A. H. Techet, and F. S. Hover, Review of experimental work in biomimetic foils, IEEE J. Oceanic Eng. **29**, 585 (2004).
[23] M. Narasimhan, H. Dong, R. Mittal, and S. N. Singh, Optimal yaw regulation and trajectory control of biorobotic AUV using mechanical fins based on CFD parametrization, J. Fluids Eng. **128**, 687 (2006).
[24] J. W. Newbolt, J. Zhang, and L. Ristroph, Flow interactions between uncoordinated flapping swimmers give rise to group cohesion, Proc. Natl. Acad. Sci. USA **116**, 2419 (2019).
[25] J. D. Zhang, H. J. Sung, and W. X. Huang, Hydrodynamic interaction of dorsal fin and caudal fin in swimming tuna, Bioinspir. Biomim. **17**, 066004 (2022).
[26] J. D. Zhang and W. X. Huang, Numerical model and hydrodynamic performance of tuna finlets, Theor. Appl. Mech. Lett. **12**, 100322 (2022).
[27] J. Wang, D. K. Wainwright, R. E. Lindengren, G. V. Lauder, and H. Dong, Tuna locomotion: A computational hydrodynamic analysis of finlet function, J. R. Soc. Interface **17**, 20190590 (2020).

[28] C. D. Wilga and G. V. Lauder, Locomotion in sturgeon: Function of the pectoral fins, J. Exp. Biol. **202**, 2413 (1999).
[29] E. M. Standen and G. V. Lauder, Hydrodynamic function of dorsal and anal fins in brook trout (*Salvelinus fontinalis*), J. Exp. Biol. **210**, 325 (2007).
[30] E. G. Drucker and G. V. Lauder, Locomotor function of the dorsal fin in rainbow trout: Kinematic patterns and hydrodynamic forces, J. Exp. Biol. **208**, 4479 (2005).
[31] G. V. Lauder and P. G. A. Madden, Learning from fish: Kinematics and experimental hydrodynamics for roboticists, Int. J. Automat. Comput. **3**, 325 (2006).
[32] D. G. Matthews and G. V. Lauder, Fin-fin interactions during locomotion in a simplified biomimetic fish model, Bioinspir Biomim **16**, 046023 (2021).
[33] P. Han, G. V. Lauder, and H. Dong, Hydrodynamics of median-fin interactions in fish-like locomotion: Effects of fin shape and movement, Phys. Fluids **32**, 011902 (2020).
[34] J. Zhu, C. White, D. K. Wainwright, V. Di Santo, G. V. Lauder, and H. Bart-Smith, Tuna robotics: A high-frequency experimental platform exploring the performance space of swimming fishes, Sci. Robot. **4**, eaax4615 (2019).
[35] G. V. Lauder, P. Madden, I. Hunter, J. Tangorra, N. Davidson, L. Proctor, R. Mittal, H. Dong, and M. Bozkurttas, Design and performance of a fish fin-like propulsor for AUVs, in *Proceedings of the 14th International Symposium on Unmanned Untethered Submersible Technology* (Autonomous Undersea Systems Institute, Lee, New Hampshire, 2005).
[36] V. Di Santo, E. Goerig, D. K. Wainwright, O. Akanyeti, J. C. Liao, T. Castro-Santos, and G. V. Lauder, Convergence of undulatory swimming kinematics across a diversity of fishes, Proc. Natl. Acad. Sci. USA **118**, e2113206118 (2021).
[37] G. V. Lauder, Function of the caudal fin during locomotion in fishes: Kinematics, flow visualization, and evolutionary patterns, Am. Zool. **40**, 101 (2000).
[38] L. Ferry and G. V. Lauder, Heterocercal tail function in leopard sharks: A three-dimensional kinematic analysis of two models, J. Exp. Biol. **199**, 2253 (1996).
[39] R. Thandiackal and G. V. Lauder, How zebrafish turn: Analysis of pressure force dynamics and mechanical work, J. Exp. Biol. **223**, jeb223230 (2020).
[40] R. Thandiackal, C. H. White, H. Bart-Smith, and G. V. Lauder, Tuna robotics: Hydrodynamics of rapid linear accelerations, Proc. R. Soc. B **288**, 20202726 (2021).
[41] K. N. Lucas, G. V. Lauder, and E. D. Tytell, Airfoil-like mechanics generate thrust on the anterior body of swimming fishes, Proc. Natl. Acad. Sci. USA **117**, 10585 (2020).
[42] R. Mittal, H. Dong, M. Bozkurttas, F. M. Najjar, A. Vargas, and A. von Loebbecke, A versatile sharp interface immersed boundary method for incompressible flows with complex boundaries, J. Comput. Phys. **227**, 4825 (2008).
[43] A. Menzer, Y. Ren, J. Guo, B. W. Tobalske, and H. Dong, Wing kinematics and unsteady aerodynamics of a hummingbird pure yawing maneuver, Biomimetics **7**, 115 (2022).
[44] C. Koehler, Z. Liang, Z. Gaston, H. Wan, and H. Dong, 3D reconstruction and analysis of wing deformation in free-flying dragonflies, J. Exp. Biol. **215**, 3018 (2012).
[45] C. C. Lindsey, Form, function, and locomotory habits in fish, in *Fish Physiology, Vol. VII: Locomotion*, edited by W. S. Hoar and D. J. Randall (Academic Press, New York, 1978), pp. 1–100.
[46] M. S. U. Khalid, J. Wang, I. Akhtar, H. Dong, M. Liu, and A. Hemmati, Larger wavelengths suit hydrodynamics of carangiform swimmers, Phys. Rev. Fluids **6**, 073101 (2021).
[47] M. S. U. Khalid, J. Wang, H. Dong, and M. Liu, Flow transitions and mapping for undulating swimmers, Phys. Rev. Fluids **5**, 063104 (2020).
[48] J. Wang, Y. Ren, C. Li, and H. Dong, Computational investigation of wing-body interaction and its lift enhancement effect in hummingbird forward flight, Bioinspir. Biomim. **14**, 046010 (2019).
[49] A. Menzer, Y. Gong, F. E. Fish, and H. Dong, Bio-inspired propulsion: Towards understanding the role of pectoral fin kinematics in manta-like swimming, Biomimetics **7**, 45 (2022).
[50] Q. Zhong, H. Dong, and D. B. Quinn, How dorsal fin sharpness affects swimming speed and economy, J. Fluid Mech. **878**, 370 (2019).

[51] J. O. Dabiri, S. Bose, B. J. Gemmell, S. P. Colin, and J. H. Costello, An algorithm to estimate unsteady and quasi-steady pressure fields from velocity field measurements, J. Exp. Biol. **217**, 331 (2013).

[52] K. N. Lucas, J. O. Dabiri, and G. V. Lauder, A pressure-based force and torque prediction technique for the study of fish-like swimming, PLoS ONE **12**, e0189225 (2017).

[53] I. Borazjani and F. Sotiropoulos, Numerical investigation of the hydrodynamics of carangiform swimming in the transitional and inertial flow regimes, J. Exp. Biol. **211**, 1541 (2008).